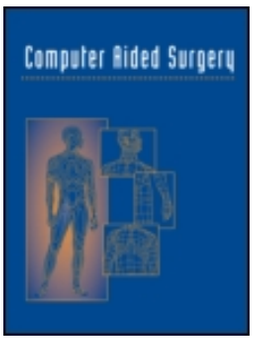

Computer Aided Surgery

ISSN: 1092-9088 (Print) 1097-0150 (Online) Journal homepage: https://www.tandfonline.com/loi/icsu20

Feasibility Study of Magnetic Resonance Imaging-Guided Intranasal Flexible Microendoscopy

Derek L. G. Hill, Line A. Langsaeter, Paul N. Poynter-Smith, Claire L. Emery, Paul E. Summers, Stephen F. Keevil, J. Paul M. Pracy, Rory Walsh, David J. Hawkes & Michael J. Gleeson

To cite this article: Derek L. G. Hill, Line A. Langsaeter, Paul N. Poynter-Smith, Claire L. Emery, Paul E. Summers, Stephen F. Keevil, J. Paul M. Pracy, Rory Walsh, David J. Hawkes & Michael J. Gleeson (1997) Feasibility Study of Magnetic Resonance Imaging-Guided Intranasal Flexible Microendoscopy, Computer Aided Surgery, 2:5, 264-275, DOI: 10.3109/10929089709148116

To link to this article: https://doi.org/10.3109/10929089709148116

Computer Aided Surgery 2:264–275 (1997)

Biomedical Paper

Feasibility Study of Magnetic Resonance Imaging-Guided Intranasal Flexible Microendoscopy

Derek L.G. Hill, Ph.D., Line A. Langsaeter, M.Sc., Paul N. Poynter-Smith, B.Sc., Claire L. Emery, B.Sc., Paul E. Summers, B.Sc., Stephen F. Keevil, Ph.D., J. Paul M. Pracy, F.R.C.S., Rory Walsh, F.R.C.S., David J. Hawkes, Ph.D., and Michael J. Gleeson, M.D., F.R.C.S.

Divisions of Radiological Sciences (D.L.G.H., L.A.L., P.N.P.-S., C.L.E., P.E.S., S.F.K., D.J.H.) and Surgery (J.P.M.P., R.W., M.J.G.), UMDS, Guy's and St. Thomas's Hospitals, London SE1 9RT, United Kingdom

ABSTRACT **Interventional magnetic resonance imaging (MRI) offers potential advantages over conventional interventional modalities such as X-ray fluoroscopy, ultrasonography, and computed tomography (CT). In particular, it does not use ionizing radiation, can provide high-quality images, and allows acquisition of oblique sections. We have carried out a feasibility study on the use of interventional MRI to track a flexible microendoscope in the paranasal sinuses. In this cadaver study, high-speed MRI was used to track a passive marker attached to the end of the endoscope.**

Automatic image registration algorithms were used to transfer the coordinates of the endoscope tip into the preoperative MRI and CT images, enabling us to display the position of the endoscope in reformatted orthogonal views or in a rendered view of the preoperative images. The endoscope video images were digitized and could be displayed alongside an approximately aligned, rendered preoperative image. Intraoperative display was provided in the scanner room by means of an liquid crystal display (LCD) projector. We estimate the accuracy of the endoscope tracking to be approximately 2 mm. Comp Aid Surg 2:264–275 (1997). ©1998 Wiley-Liss, Inc.

Key words: **interventional MRI, endoscope, nasal sinuses, paranasal sinuses, tracking, registration, distortion**

INTRODUCTION

The ability of MRI to provide both anatomical and functional information without exposure of patients and staff to ionizing radiation makes interventional MRI an attractive goal. The superior soft tissue resolution of MRI, along with its multiplanar imaging capability, make it an interesting alternative to CT, X-ray fluoroscopy and ultrasonography. Recent advances in MRI hardware, and alternative k-space sampling algorithms,[1,6,8,28,29,31] have allowed much faster scanning times. The speed of scanning has now reached the stage where nearly real-time imaging is a possibility.

Proposed uses for interventional MRI include percutaneous breast biopsies,[4] aspiration cytology, thermotherapy,[10,23,24,27,30] intravascular procedures,[11,15,16,19,33] interstitial focused ultra-

Received original May 28, 1997; accepted August 19, 1997.

This paper is based on a presentation at the Visualization in Biomedical Computing International Conference held in Hamburg, Germany, September, 1996.

Address correspondence/reprint requests to: Dr. Derek L.G. Hill, Radiological Sciences, UMDS, Guy's Hospital Campus, St. Thomas' Street, London SE1 9RT, U.K. E-mail: d.hill@umds.ac.uk.

sound,[22] and needle placement,[14,17,18] as well as endoscopic imaging.[5] Many of these capabilities have been demonstrated only ex vivo.

Conventional endoscopic sinus surgery uses rigid endoscopes to view the sinuses and osteomeatal complex. There is a small but significant risk of damage to structures that are in close relation to the sinuses. At particular risk are the orbital contents (including the optic nerve), the cribiform plate, the skull base, and the internal carotid arteries, which indent the roof of the sphenoid sinus. Access to the sinuses can be limited by the use of rigid endoscopes in such a confined space, and it is sometimes necessary to use 30°- and 70°-angled lenses to look into the maxillary and frontal sinuses. The use of angled lenses requires considerable experience and expertise, because the view afforded is disorienting. Access and safety could be improved by the use of a flexible endoscope, but in this case tracking would be helpful to provide orientation within the sinuses. A conventional localizer (e.g., mechanical arm) cannot be used to track a flexible tool, and CT, fluoroscopy, and ultrasound are all unsatisfactory for real-time tracking of a tool that can move in three dimensions (3-D) through air and tissue. The objective of the work described herein was to demonstrate the feasibility of tracking a flexible microendoscope using an MRI scanner and using image registration techniques to relate video images acquired with the endoscope to high-quality CT and MRI images acquired before the intervention.

MRI Compatibility

Ferromagnetic materials should be kept well away from MRI systems; they are attracted to the bore of the magnet and can be dangerous to both patient and clinician. Other materials are characterized by their magnetic susceptibility, related to their inherent magnetic properties. Any material that has magnetic susceptibility different from that of the tissues being imaged will create a local geometric and intensity distortion within the image (especially when using gradient echo imaging). Surgical instruments introduced into the patient should, therefore, have a susceptibility as close as possible to that of tissue. The image degradation caused by susceptibility differences is dependent on the imaging sequence being used. This degradation is minimized using spin-echo sequences, in which spin dephasing caused by susceptibility differences is rephased using a 180° radiofrequency (RF) pulse.

MRI Visibility

The instruments must be visible in the MRI scan. Solid objects made of metal alloys (e.g., most surgical instruments) normally appear as dark signal voids in MRI and are often surrounded by a wider area of signal loss resulting from susceptibility differences. When introduced into a tissue that appears bright on MRI, they can be clearly seen. However, the size and shape of signal voids caused by magnetic susceptibility can change with orientation with respect to the magnetic field. In addition, not all of the structures within a patient are bright on MRI, for example, the air sinuses, bone, and some fluids are dark in certain MRI sequences. A signal void would in these cases be indistinguishable from its surroundings. Adding a bright marker, for example, one containing an appropriate concentration of the paramagnetic contrast material gadolinium DTPA (Magnevist; Schering AB, Berlin, Germany), to the instrument can make it visible when surrounded by low-intensity tissue or air,[11] but the instrument can cease to be visible if moved into a region where the surrounding tissue produces an MRI signal similar to that of the marker. These problems can be overcome by using an active marker that incorporates a small RF receive or send/receive coil surrounded by MRI-visible material.[2,6,12,13,20,21] Very simple imaging sequences, made up of a small number of projections, can be used to identify the 3-D position of these active markers. Metal RF coils can, however, cause local heating, which can in turn cause additional as yet unquantified trauma to the patient. Maier et al.[18] have assessed the increase in tissue temperature that coils of this sort generate. Heating is caused primarily by the RF field, with a doubling of the RF field amplitude leading to a fourfold increase in tissue temperature. It is also dependent on magnetic field strength and the sequence used, with the greatest effects seen with turbo spin echo sequences, with high-field magnets, and with the catheter oriented in the plane perpendicular to the direction of the static magnetic field. In the work described herein, we have chosen to use a passive, high-intensity marker owing to concerns about the clinical safety of active RF coils inserted into the tissues of the patient.

MATERIALS AND METHODS

Design of Passive Endoscope Marker

To track a bright passive marker, it is necessary to select the optimal concentration of the marker material. We use gadolinium DTPA (Gd-DTPA)

with the fast MRI sequence that is run during the intervention. Concentrations of between 0 and 30 mmol liter^{-1} Gd-DTPA were placed in 20 ml plastic vials, and imaged using a turbo spin echo (TSE) pulse sequence [T_R = 106 msec, T_E = 11 msec, turbo factor (TF) = 8]. The TF describes the number of lines in k-space that are acquired following a single excitation pulse using multiple phase encoding gradients. The marker concentration providing the best signal intensity depends on the sequence. We chose the concentration that gave the highest intensity for the fast MRI sequence used for this preliminary "interventional" scan. The degradation in signal intensity caused by partial volume effect and susceptibility artifacts was then assessed by placing the optimal concentration of marker fluid into plastic tubing and then reimaging. Several types of biocompatible, clinically used tubing materials with different diameters and wall thicknesses were used for this purpose. The intensity of the marker relative to surrounding tissue for the selected pulse sequence was then assessed using a fresh porcine cadaver.

Modification of the Microendoscope for MRI Compatibility

We constructed a modified microendoscope, using the 6,000-pixel imaging fibers and the illumination fibers of an Omegascope OM2/070 flexible microendoscope (Omega Universal Technologies Ltd., London, U.K.). This was made MRI compatible by encasing it in a biocompatible polythene catheter with an outer diameter of 2.3 mm. The final 2 cm of the catheter had the guidewire and working channels filled with Gd-DTPA contrast agent, at the concentration determined from the experiments described below, and the ends were sealed with wax.[7] A single-chip color charge-coupled device (CCD) camera was attached to the endoscope eyepiece and could operate satisfactorily in the bore of a 1.5 T MRI scanner. The video output was connected, via a long video lead, to a SunVideo (Sun Microsystems, Mountain View, CA) frame grabber in a workstation in the scanner control room.

Construction of the MRI-Compatible Light Source

An MRI-compatible endoscope light source was constructed. The light source was housed in an aluminum alloy box, with a DC rather than an AC power input, avoiding the need for the light source to contain a transformer. Long power cables were used to keep the power supply transformer outside the RF shield. A 150 W, 15 V reflective xenon bulb was used to supply light onto the ends of the illumination fibers. A small 6 V fan was attached to the side of the box to cool the bulb. Although the fan contained a small amount of ferromagnetic material, the light source could be attached to the scanner couch, approximately 50 cm away from the magnet bore, without being attracted into the scanner or degrading the images. The endoscope was connected to the light source using a machined polyvinyl chloride (PVC) socket and was protected from the heat of the bulb by heat-absorbing glass.

Display of Images in the Scanner Room

A 1,024 × 768-pixel, active color LCD projector panel was used to project video from the endoscope and processed images displayed on a Sun workstation into the scanner room, where it could be seen by the clinician. The projector could be placed in a field strength of less than 1 mT, with the images projected onto a screen placed in an arbitrary field strength.

Cadaver Experiments

The expected clinical protocol for the use of the system is described below. This protocol was tested using a primate cadaver head. This primate had been sacrificed for a separate research project involving removal of the temporal bones.

"Preoperative" Imaging

CT scanning is the modality of choice for visualizing the paranasal sinuses and osteomeatal complex. Preoperative imaging was carried out using a Philips SR7000 spiral CT scanner (Philips Medical Systems, Best, The Netherlands). Sixty-one slices, 1.5 mm thick, with a field of view of 200 mm and a 512^2 matrix, were acquired. A high-resolution preoperative T_1-weighted spin echo (SE) MRI scan was also acquired using the 1.5 T Philips Gyroscan ACS-II (Philips Medical Systems). This scan was registered to the CT scan using the fully automatic voxel similarity measure algorithm based on the mutual information of the joint probability distribution.[25]

"Interventional" Imaging

Prior to the interventional scan, some dissection of the primate cadaver was performed by a surgeon to allow access to the maxillary sinus. This is the same procedure as is carried out in conventional sinus surgery, and we envision that, in clinical use, this would be done while the patient is lying on the scanner couch. The cadaver head was then placed in the scanner, and the endoscope

was inserted into the nasal sinus. The orientation of the endoscope was ascertained before insertion so that the operator could orient himself while entering the sinus system. The marker attached to the flexible microendoscope was visualized within the sinus system using the TSE sequence (T_R = 106 msec, T_E = 11 msec, TF = 8) for which the marker concentration had been optimized. These "interventional" images were registered to the preoperative MRI, and hence to the preoperative CT images, by optimizing the correlation coefficient of the joint probability distribution.[26] Initial experimentation indicated that, for our data, the correlation coefficient is more robust with regard to variation in the starting estimate of the registration than the mutual information. This registration took approximately 1 min on a SunSparc Ultra 1/140 workstation with a starting estimate of approximately 10 mm translation and 10° rotation from the registration solution.

Accuracy Considerations

System performance is an important consideration in these experiments. To test the reliability of the techniques used, the various sources of error had to be identified and quantified. The accuracy with which one can determine the position of the endoscope tip depends on 1) the delineation of the marker, 2) the registration accuracy for both MRI to CT and interventional MRI to preoperative MRI, and 3) the distortion of both MRI and endoscope images. These issues will be dealt with in the subsequent sections.

Acquisition of High-Speed MRI

We acquired two further MR data sets: first, a high-resolution T_1-weighted TSE scan (T_R = 235 msec, T_E = 40 msec, TF = 5) with a 256^2 matrix and 2-mm-thick slices, with a time of approximately 19 minutes for 73 slices, and, second, 21 slices of a low-resolution TSE sequence (T_R = 200 msec, T_E = 21 msec, TF = 10), with a slice thickness of 5 mm, a one-half scan factor of 0.625, a k-space reduction factor of 50%, and a rectangular field of view (FOV) of 70% in the phase-encoding direction; the scan time for this sequence was approximately 2 min.

Delineation of the Marker

The identification of the marker tip coordinates depends on the pixel size of the image. If the diameter of the marker is less than the pixel diameter, the localization accuracy is no better than $\pm a/2$, where a is the pixel dimension. If, on the other hand, the marker diameter is greater than the pixel diameter, and we can assume a symmetric point spread function (PSF), the position of the marker may be found to an accuracy better than $\pm a/2$ by using a center of gravity operator. However, the center of gravity operator is sensitive to image intensity modulations, which are likely to be present in the vicinity of the marker. This modulation can be due to susceptibility artifacts from the endoscope tip and noise from the rapid sequence used as well as signal from underlying and overlying structures.

Preoperative Registration

There are two stages in the registration method described above, registration of the preoperative CT to preoperative MRI and registration of the interventional MRI to preoperative MRI. We have not carried out an assessment of the registration of the preoperative MRI to the preoperative CT for this paper. However, our group participated in a multicenter trial evaluating the accuracy of our automated registration algorithm (described by West et al.[32]). In this blinded multicenter trial, the median registration error when registering a CT image to a T_1-weighted MRI scan using this algorithm was found to be 1.2 mm. We can expect to achieve a similar level of accuracy in our registration procedure using the MRI and CT scans described herein.

Intraoperative Registration

One way to ensure that "interventional" imaging sequences are rapid enough for clinical use is to reduce the FOV, updating only the information contained within a small volume of the object. This technique is used in the near-real-time sequence "LoLo,"[29] which combines a rectangular FOV with turbo spin echo acquisition, one-half scan, and k-space reduction. This type of rapid sequence seems appropriate for tracking a small object in a restricted area.

To test the accuracy and robustness of the registration algorithm when registering a restricted volume, low-resolution data set to a high-resolution, full-head data set from the same image modality, we applied the following protocol. We truncated the "interventional" low-resolution data set along the slice select axis into increasingly smaller units (multiples of the slice thickness) and also reduced the matrix in the x and y directions from 256^2 to 128^2. Each of these truncated subvolumes was then registered to the preoperative high-resolution MRI data set by optimizing the correlation coefficient of the two

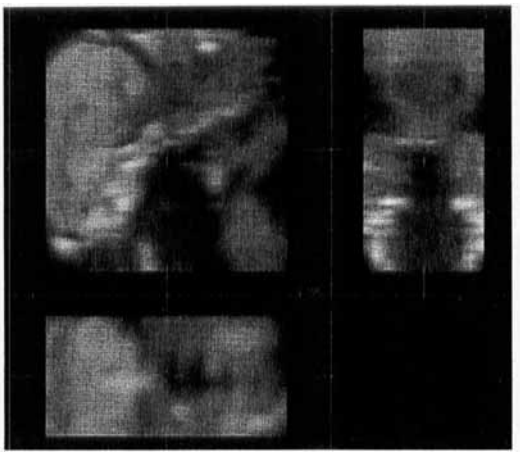

Fig. 1. One of the subvolumes from the "interventional" scan: 128^2 matrix with 10 slices each of 5 mm thickness (90 × 90 × 50 mm). The image shows sagittal (the plane of the acquired slice) in the top left corner, axial (top right), and coronal (bottom left) views. The subvolume is taken from the middle of the volume, showing the upper spinal cord and oral cavities. The slices were interpolated by linear interpolation for display purposes.

images, producing a "subvolume registration transformation." A sample subvolume is presented in Figure 1. A registration of the entire low-resolution MRI data set to the high-resolution MRI data set was used as a pseudo-"gold standard" registration transformation for this experiment. The subvolumes of the low-resolution MRI sequence were each registered to the high-resolution MRI scan, with a starting estimate given by the gold standard transform incorporating a translation error of up to 5 mm in the x, y, and z directions.

Registration errors were assessed at nine points distributed around the high-resolution MRI volume. The points were chosen in the frontal lobe, on the postcentral gyrus, cerebellum, middle nasal region, left maxillary sinus, right maxillary sinus, lower jaw, and lower nasal region, and in the medulla oblongata. The precise anatomical position of these points is not critical, but it is important that they are spread throughout the volume of interest in order to characterize the rotational as well as the translational registration errors.

We calculated a 3-D displacement for each of the nine selected points during the registrations. This was done by comparing the coordinates for each point from the subvolume registration and the gold standard registration. The displacement was used as a measure of registration error at that point. Each point has coordinates (x, y, z) in the high-resolution MRI scan to which the other scans were registered. This point first underwent the rotation and then the translation of the gold standard transformation, giving it the new coordinates (x′, y′, z′) by

$$(x', y', z') = R_g(x, y, z) + T_g$$

where R_g is the gold standard rotation matrix and T_g is the gold standard translation vector. This calculation was also performed on the same point (x, y, z) in the reference image using the subvolume registration transformation. This gives the new point coordinates (x″, y″, z″) from

$$(x'', y'', z'') = R_s(x, y, z) + T_s$$

where R_s, is the subvolume rotation and T_s is the subvolume translation. The displacement between the point transformed using the subvolume transformation and the same point transformed with the gold standard transformation is thus given by the length of the vector separating points (x′, y′, z′) and (x″, y″, z″). This displacement, which is the error at that point, was calculated for all nine points for each subvolume registration transformation.

Distortion

There are two main sources of image distortion in this system, namely MRI distortion and video (or endoscope) distortion. The first is due to several phenomena, including gradient nonlinearities, chemical shift, and pixel scaling errors in the MRI system. In our experience, pixel scaling errors can dominate in sequences with strong readout gradients, with mean errors greater than 1% and sometimes as much as 7%. MRI scaling errors, unlike other forms of MRI distortion, can be relatively easily corrected using phantom measurements. The video distortion can be evaluated by a calibration of the optical characteristics of the lens. With its wide viewing angle, the endoscope lens presents quite large distortions. The barrel distortion was characterized by imaging a test object consisting of straight lines separated by 2 mm in a grid pattern. The coordinates of the intersections between lines on the grid seen through the endoscope image are measured. The radial distance to the observed intersection from an estimated center of distortion is calculated using Pythagoras' theorem. The corrected radial distance can then be given as a polynomial of

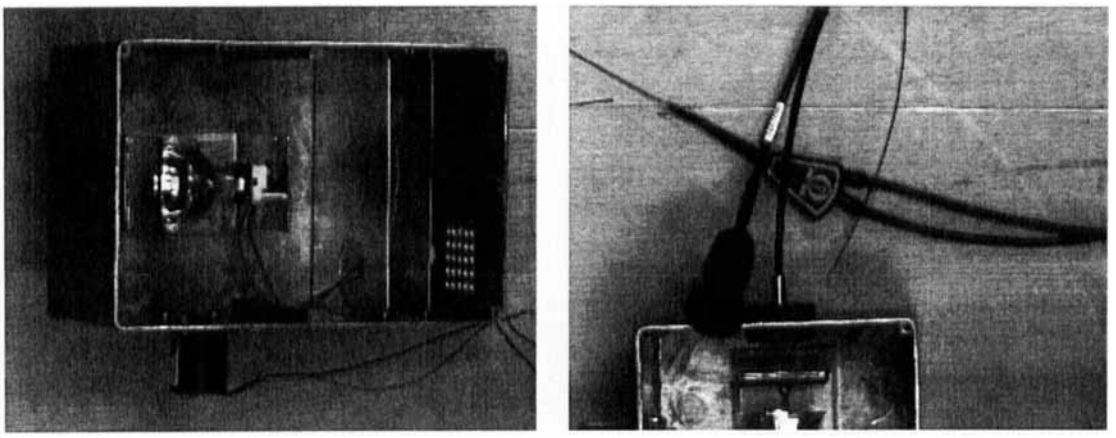

Fig. 2. Endoscope light source with lid removed (left) and attached to endoscope (right).

the distorted radial distance. By optimizing the polynomial coefficients and estimating the center of distortion, the correction factors that characterize the system can be determined.[9] These correction factors can then easily be applied to any image taken with the same system. By *system* we mean a specific configuration of lens and optics in the endoscope system. New calibrations must be performed for any change in the configuration, such as movement of individual optics with relation to each other. This 2-D distortion correction of a 3-D object assumes circular symmetry, and precautions should be taken when interpreting structures, especially in the periphery of the image.

RESULTS

Design of Endoscope

The concentration of Gd-DTPA that produced the highest intensity signal when imaged with the TSE sequence described above was 7.5 mmol liter^{-1}. The intensity was reduced dramatically if the tube encasing the marker had a diameter less than 1 mm or if the marker volume dropped below 5 ml. The MRI-compatible light source is shown in Figure 2.

Cadaver Experiment

Orthogonal views from the "preoperative" CT of the primate head are shown in Figure 3. The nasal sinuses are seen very clearly. Figure 4 shows the preoperative MRI, described above, with the thresholded bone boundary from CT overlaid.

Figure 5 shows a composite view comprising orthogonal views, along with a rendered image showing the relationship between the endoscope localized in the high-speed TSE (T_R = 106 msec, T_E = 11 msec, TF = 8) imaging sequence and the preoperative CT scan (Fig. 6). In the orthogonal views, the endoscope marker is shown as a thresholded boundary overlaid on the CT image. In the perspective-rendered scene, the endoscope is shown as a dark cylinder protruding from the nasal cavity.

Although the image quality of the fast sequence was much reduced, the endoscope tip could be clearly seen. The contrast to noise ratio was not always sufficient to locate the marker by thresholding alone, so user interaction was required to identify the endoscope tip and orientation.

After calculation of the registration transform relating the interventional MRI to the preoperative CT and MRI, the position of the endoscope tip could be displayed in orthogonal slices. With knowledge of the position of the endoscope tip relative to the preoperative CT, it is also possible to produce a rendered scene of the CT data along the axis of the endoscope. A frame of the video endoscope image shown alongside a CT image (rendered using the Vislan software[3]) obtained from the same anatomical position is presented in Figure 7. However, it should be stressed that this initial endoscope image was not distortion corrected. To align a rendered image with an endoscope image accurately, it is necessary to calibrate the video perspective geometry and correct for distortion as discussed above.

Accuracy Measurements

The results presented in Figure 8 show a decrease in registration errors of low-resolution MRI to

high-resolution MRI for an increasing number of slices in the subvolume. The error bars represent the spread in point transformation for the different points expressed as 1 standard deviation (SD). There is also an overall reduction in spread of the registration errors when the number of slices increases. For all the studies performed, the subvolume registration transformations have a maximal error of 1.61 ± 0.56 mm (1 SD). We performed a single-tailed t-test in order to determine whether this number was significantly different to the overall registration error. Using a confidence interval of 95%, we found the result to be nonsignificant. The results suggest that a small intraoperative MRI data set of image quality and size equivalent to those of the TSE subvolume considered here can be registered to a high-resolution preinterventional MRI by using this registration algorithm with an accuracy between 1 mm and 2 mm.

From our results, there seems to be only slight improvement in the registration accuracy of low-resolution MRI to high-resolution MRI for an increasing number of slices (Fig. 8). Even for a single 5 mm slice in a 128^2 matrix, which encompasses much of the head in two directions (about 60 %), but limited information in the third direction, the mean registration error for nine points chosen in the data set, all from different structures, is 1.52 mm, with a standard deviation of ±0.25 mm.

Figure 9 shows 1) an uncorrected and 2) a distortion-corrected endoscope view of a calibration grid. During conventional endoscopy, the image errors introduced by imperfections in the endoscope optics do not seem to have a great deal of influence on the accurate diagnosis and treatment of infections and/or lesions within the sinuses, because surgeons (at least those at our institution) are used to the degraded image quality from endoscopes, especially in the periphery of the lens, and it is standard practice to take care to avoid any complications that might be introduced due to these problems.

DISCUSSION

The results show that it is possible to locate the tip of a flexible endoscope in a fast SE sequence with an accuracy of approximately 2 mm and to obtain video pictures from the same location via the endoscope itself. Current surgical guidance systems, using mechanical arms, ultrasound, or optical tracking, are capable of localizing the position of a rigid pointer or rigid surgical instrument with respect to preoperative images. These

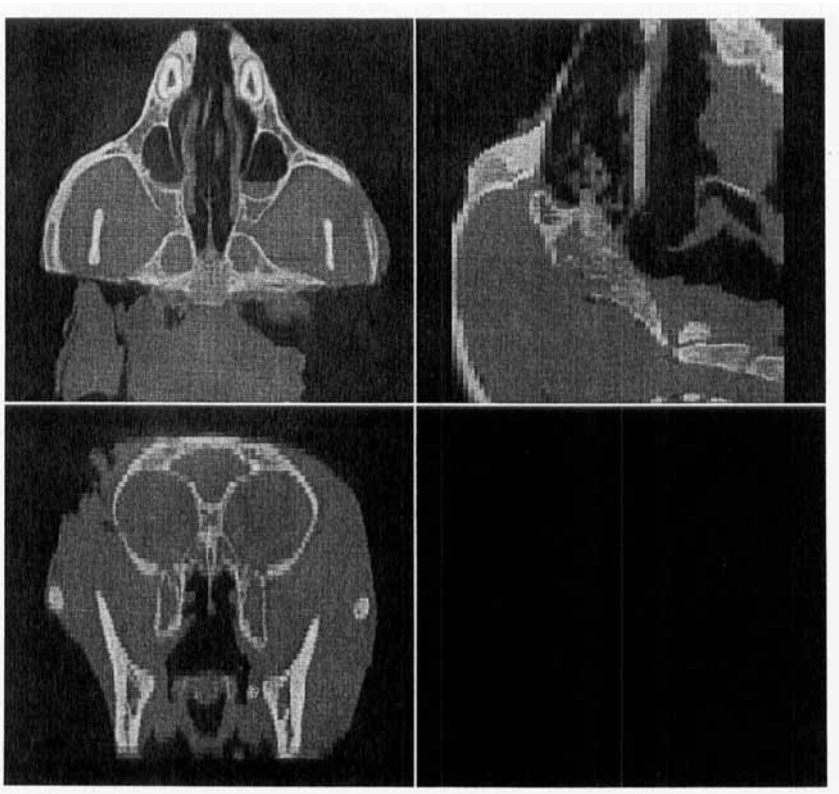

Fig. 3. Orthogonal views from the CT scan of a primate cadaver described in the text.

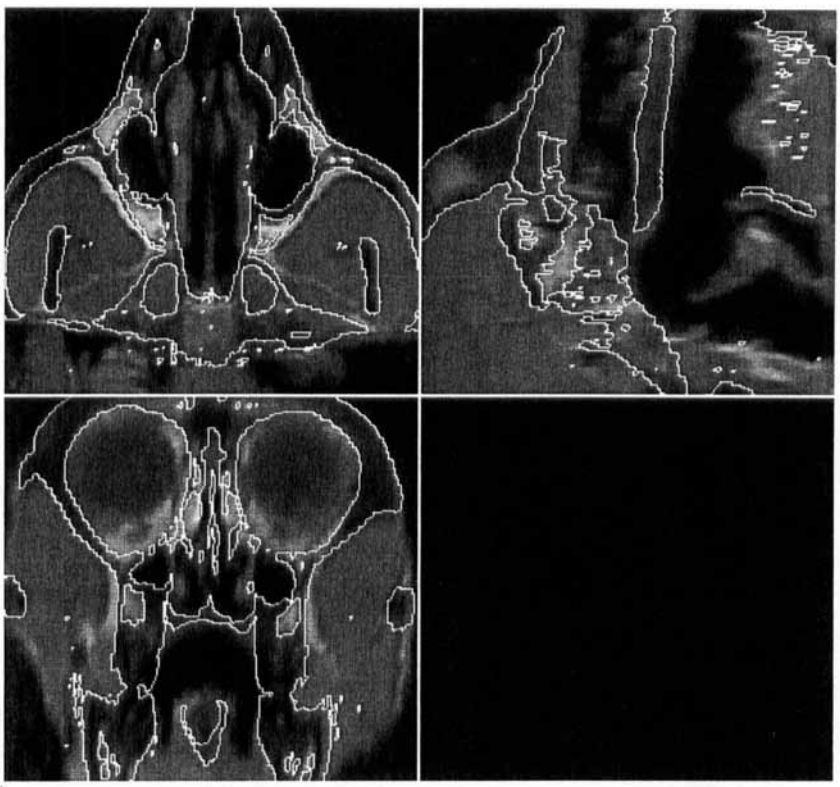

Fig. 4. Orthogonal views from the MR, with the thresholded bone boundary from CT overlaid. Scan sequences described in the text.

guidance systems are not appropriate for use with flexible instruments or when significant tissue deformation is expected during the course of the procedure.

Interventional radiology is also usually unsatisfactory for tracking flexible instruments. Conventional X-rays provide poor contrast and, even with a biplane system, only limited 3-D information. Interventional CT or conventional ultrasound provides only a single plane, which is insufficient for tracking flexible tools. Three-dimensional ultrasound might have applications in some parts of the body, but the mixture of air, bone, and soft tissue in the paranasal sinuses makes ultrasound unsuitable for tracking flexible tools in this application.

We have shown that interventional MRI can be used to track flexible instruments, in a manner analogous to the use of a conventional guidance system. By means of voxel-based registration algorithms, one can display the position of the instrument in the context of the preoperative images. The accuracy with which the interventional scans can be registered to the preoperative scans suggests that near-real-time scan sequences using "zooming" techniques such as LoLo[29] can be used without introducing large registration errors. In our application, it would be advantageous to automate the tracking of the endoscope. This might be done by tracking the passive marker in a series of fast images or by means of safe active markers.

Further studies on the accuracy of position measurements in the MRI will support the choice of a minimal "interventional" volume that is clinically acceptable. These measurements were performed using a fast sequence scan with 5-mm-thick slices as described above. The truncated volumes are generated by cutting off pixels in two directions and reducing the number of slices in the sagittal direction. The low-resolution sequence used for these experiments was designed to provide resolution and contrast similar to those of a one-shot single bulk volume acquisition such as LoLo while providing us with the flexibility to change the volume used for registration. Our results might not be directly applicable to these interventional sequences in all situations. The median error for the CT to MRI registration can be estimated to be on the order of 1.2 mm with reference from accuracy discussed above. When considering all the different sources of positioning error,

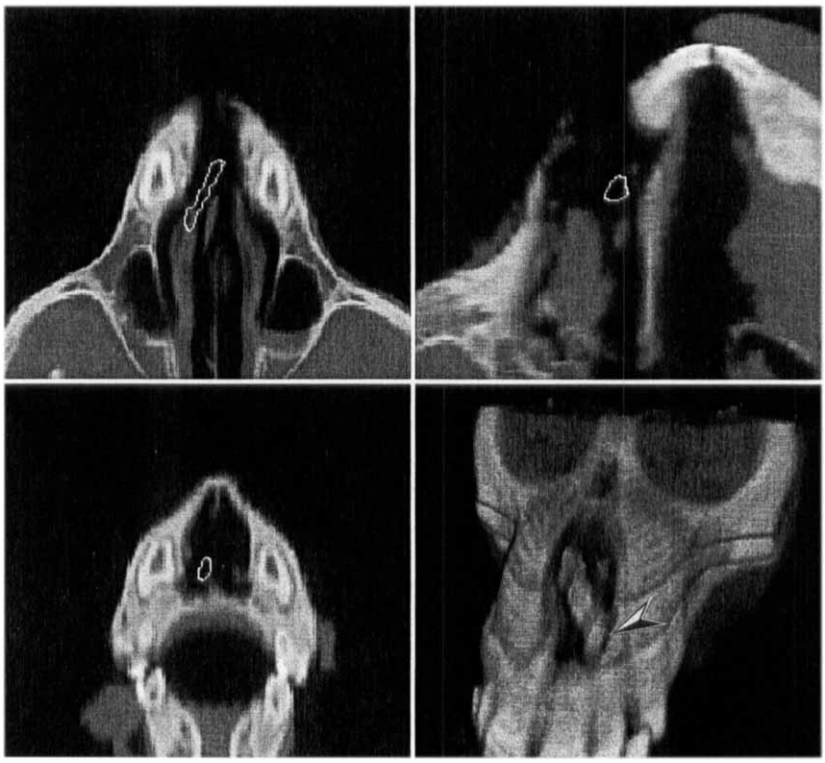

Fig. 5. Orthogonal views and rendered scene from the CT scan. The thresholded boundary of the endoscope marker from the registered MR is overlaid in the orthogonal CT views, and the endoscope is displayed as a dark cylinder protruding from the nose in the perspective rendered view (arrow). The images are from the scans described in the text.

the possible influence of imperfect pixel scaling in the scanner must also be taken into account.

The endoscope image can be displayed alongside preoperative images, indicating the position of the endoscope tip at all times during the intervention. The preoperative images can be displayed either as reformatted axial, coronal, and sagittal planes or as perspective rendered views. The projection of these images on the LCD screen in a suitable position in the scanning room permits effective guidance for the surgeon without having to move from the working position.

Fig. 6. Turbo spin echo image (T_R = 106 msec, T_E = 11 msec, TF = 8) showing endoscope marker visible with high intensity entering the nasal cavity of a porcine cadaver.

To relate more accurately the rendered views of the preoperative images to the endoscope images, it is also important to calibrate the endoscope optics and either correct for the optical distortion in the endoscope images as described above or alternatively apply the optical distortion to the rendered images. The second approach is more straightforward in computation but could give confusing and, indeed, incorrect views. Relatively powerful computational equipment makes the first approach feasible.

In this paper, we have described the use of fast MRI for tracking a flexible endoscope in the paranasal sinuses and the use of an image registration algorithm to make it possible to display the position of the tracked endoscope overlaid on preoperative images of the same patient. This technique would potentially be applicable to the tracking of flexible instruments in many other procedures, for

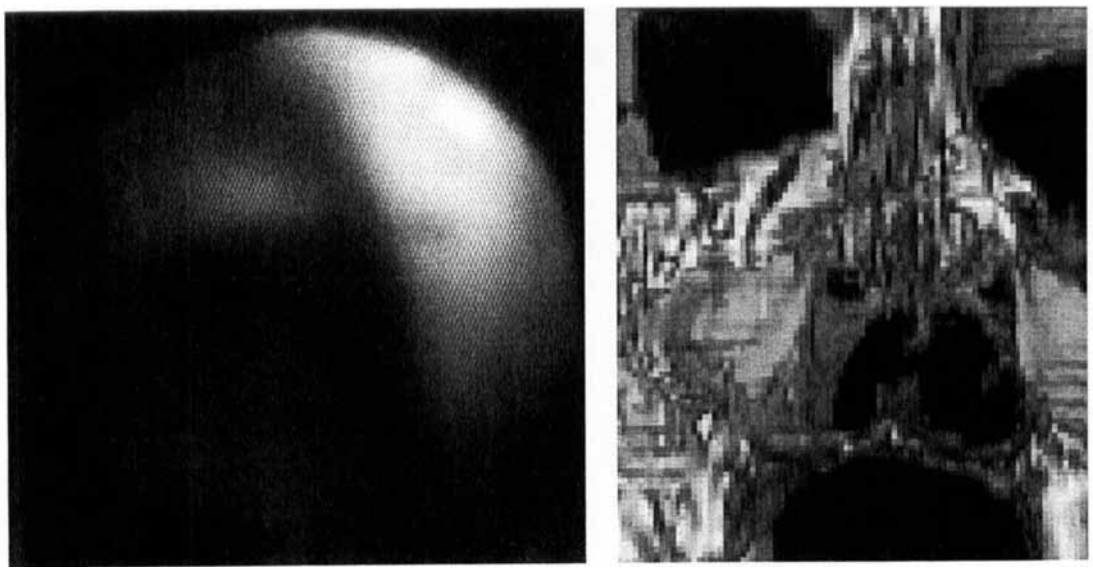

Fig. 7. Frame-grabbed videoendoscopy image, which is not distortion corrected (see text) alongside a rendered CT view along the same axis as the endoscope marker. The rendered view is produced using a parallel projection and has a much larger field of view than the video image. The aim is to provide context for the endoscope image, rather than generate a corresponding rendered view.

example, endoscopes in other regions of the body, catheters in endovascular interventions, and flexible needles in biopsies. In all applications, it is necessary for the instruments to be modified so that they are MRI compatible and MRI visible as described in our current application.

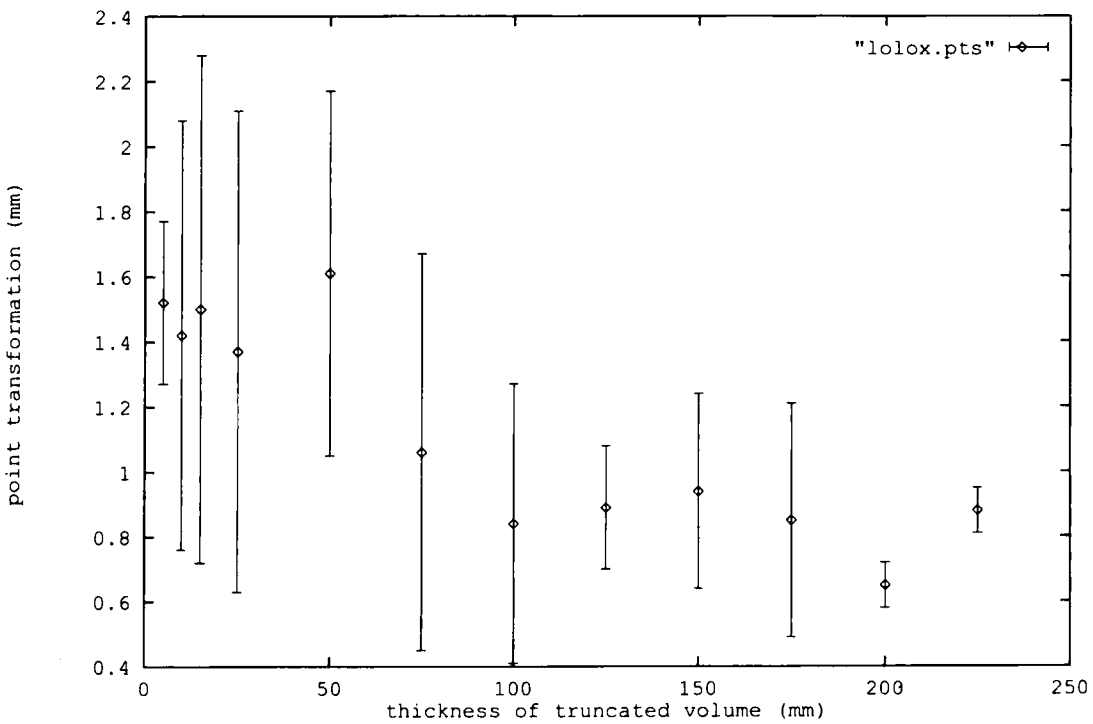

Fig. 8. Mean point transformation for nine selected points is presented here for the different low-resolution MR subvolumes registered to the high-resolution MR scan. The errors are given as ±1 SD. Points were chosen from fat, white matter, grey matter, air, and bony areas. The smallest volume measures 5 × 90 × 90 mm.

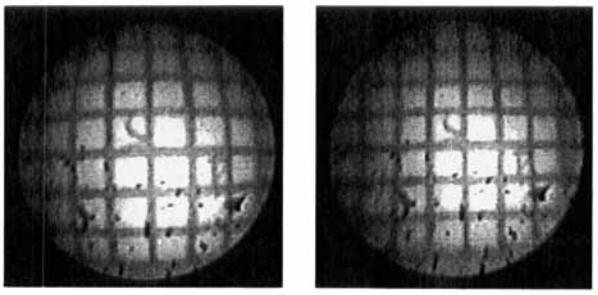

Fig. 9. Views of a calibration grid through the endoscope. The barrel distortion is quite significant (left) for this small-diameter lens. A distortion-corrected image of the grid is shown on the right.

ACKNOWLEDGMENTS

We are grateful for the assistance of Dr. Daryl DeCuhna, Mr. Julian McGlashan, Dr. Eddie Boyd, and Mr. John Walliker in experimental design and equipment configuration. We are also grateful to the Medical Physics workshop for assisting in construction of equipment and U.K. EPSRC (GR/J90183) for their support.

REFERENCES

1. Alexander AL, Buswell HR, Parker DL (1996) A time-efficient k-space sampling scheme for 3D fast spin echo. Proc Int Soc Magn Reson Med, p 1466.
2. Busch MJH, Wendt M, Melzer A, Wetzler R, Lerchner H, Groenenmeyer DHW (1997) Active tip tracking as a control method for the positioning of medical instruments during MR-guided interventional procedures. Proc Int Soc Magn Reson Med, p 1922.
3. Colchester ACF, Zhao J, Holton-Tainter KS, Henri CJ, Maitland N, Roberts PTE, Harris CG, Evans RJ (1996) Development and preliminary evaluation of VISLAN, a surgical planning and guidance system using intra-operative video imaging. Med Image Anal 1:73–90.
4. DeSouza NM (1995) MRI directs localisation, biopsy of breast lesions. Diagn Imag Eur, Feb, pp 40–43.
5. DeSouza NM, Hall AS, Coutts GA, Puni R, Taylor-Robinson SD, Young IR (1995) Endoscopic magnetic resonance imaging of the upper gastrointestinal tract using a dedicated surface receiver coil. Proc Soc Magn Reson, p 1157.
6. Dumoulin CL, Souza SP, Darrow RD (1993) Real time position monitoring of invasive devices using magnetic resonance. Magn Reson Med 29:411–415.
7. Emery CL, Hill DLG, Keevil SF, Summers PE, McGlashan JA, Walsh R, Diamantopoulos C, Liepens PJ, Hawkes DJ, Gleeson MJ (1995) Preliminary work on MR guided flexible micro-endoscopic sinus surgery. Proc Soc Magn Reson, p 1158.
8. Friebe MH, Brusch M, Hellwig S, Wentz KU, Groenmeyer DHW (1994) Keyhole sequence with rotational K-space updating as a means of fast high quality low-field interventional MR imaging. Proc Soc Magn Reson, p 161.
9. Haneishi H, Yagihashi Y, Miyake Y (1995) A new method for distortion correction of electronic endoscope images. IEEE Trans Med Imag 14:548–555.
10. Kettenbach J, Silverman SG, Kuroda K, Nakajima Y, Zientara GP, Saiviroonporn P, Hata N, Morrison PR, Hushek SG, Gering D, Black PML, Kikinis R, Jolesz FA (1997) Real time monitoring and quantitative analysis of MR-guided laser ablation. Proc Int Soc Magn Reson Med, p 523.
11. Kochli VD, McKinnon GC, Hofmann E, von Schulthess GK (1994) Vascular interventions guided by ultrafast MR imaging: Evaluation of different materials. Magn Reson Med 31:309–314.
12. Ladd ME, Erhart P, Godhe SC, Debatin JF, McKinnon GC (1996) Guidewire antennas for MRI-guided vascular interventions. Proc Int Soc Magn Reson Med, p 1736.
13. Ladd ME, Erhart P, Zimmermann G, Debatin JF, McKinnon GC (1996) MR trackable vascular guidewire. Eur Soc Magn Reson Med Biol, p 264.
14. Leung DA, Debatin JF, Wildermuth S, Heske N, Dumoulin CL, Darrow RD, Hauser M, Davis CP, von Schulthess GK (1995) Real-time biplanar needle tracking for interventional MR-imaging procedures. Radiology 197:485–488.
15. Leung DA, Wildermuth S, Debatin JF, Holtz D, Dumoulin CL, Darrow RD, Hofmann E, Schulthess GK (1995) Active visualisation of intravascular catheters with MRI: In vitro and in vivo evaluation. Proc Soc Magn Reson, p 428.
16. Leung DA, Debatin JF, Wildermuth S, McKinnon GC, Holtz D, Dumoulin CL, Darrow RD, Hofmann E, von Schulthess GK (1995) Intravascular MR tracking catheter: Preliminary experimental evaluation. Am J Roentgenol 164:1265–1270.
17. Lewin JS Duerk JL, Haaga JR (1995) Needle localisation in MR guided therapy: Effect of field strength, sequence design, and magnetic field orientation. Proc Soc Magn Reson, p 1155.
18. Maier SE, Wildermuth S, Darrow RD, Watkins RD, Debatin JF, Dumoulin CL (1995) Safety of MR tracking catheters. Proc Soc Magn Reson, p 497.
19. Martin AJ, Henkelman RM (1994) Intravascular MR imaging in a porcine animal model. Magn Reson Med 32:224–229.
20. McKinnon G (1995) Tracking and monitoring the effects of interventional MR instruments. Proc Soc Magn Reson, p 490.
21. McKinnon GC, Debatin JF, Leung DA, Wildermuth S, Holtz DJ, von Schulthess GK (1996) Towards active guidewire visualization in interventional magnetic resonance imaging. Magn Reson Mater Phys Biol Med 4:13–18.
22. Moonen CTW, Madio D, Olsen A, DesPres D, van Gelderen P, Fawcett T, Holbrook N (1997) On the

feasibility of MRI guided focused ultrasound for local induction of gene expression. Proc Int Soc Magn Reson Med, p 526.

23. Moriarty JA, Chen JC, Purcell CM, Peters RD, Hinks RS, Ang LC, Henkelman RM, Plewes DB, Bronskill MJ, Kucharczyk W (1997) MRI monitoring of interstitial microwave-induced heating and thermal lesions in rabbit brain in vivo. Proc Int Soc Magn Reson Med, p 267.
24. Roberts HRS, Paley M, Lees WR, Hall-Craggs MA, Brown SG (1995) MR Control of laser destruction of hepatic metastases. Proc Soc Magn Reson, p 1590.
25. Studholme C, Hill DLG, Hawkes DJ (1996) Automated 3D registration of MR and CT images of the head. Med Imag Anal 1:163–175.
26. Studholme C, Hill DLG, Hawkes DJ (1997) Automated three-dimensional registration of magnetic resonance and positron emission tomography brain images by multiresolution optimisation of voxel similarity measures. Med Phys 24:25–35.
27. Tacke J, Adam G, Speetzen R, Brucksch K, Heschel I, Rau G, van Vaals JJ, Gunther RW (1997) MRI guided interstitial cryotherapy of the liver with a new MRI compatible Nitrogen supplied cryoprobe. Proc Int Soc Magn Reson Med, p 268.
28. Thedens R, Gold GE, Irarrazabal P, Nishimura DG (1996) Fast 3D imaging with a short Readout short TE cones trajectory. Proc Int Soc Magn Reson Med, p 113.
29. Van Vaals JJ, Van Yperen GH, Hoogenboom TLM, Duijvestijn MJ (1994) Real time MR imaging using LoLo (local look) method for interactive and interventional MR at 0.5T and 1.5T. Magn Reson Imag 4:38.
30. Vogl TJ, Mack MG, Scholz WR, Muller P, Weinhold N, Philipp C, Bottcher H, Roggan A, Felix R (1996) MR imaging-guided laser-induced thermotherapy. Min Invas Ther Allied Techn 5:243–248.
31. Wendt M, Busch M, Lenz G, Seibel RM, Groenemeyer DH (1996) Dynamic tracking algorithm for interventional MR-imaging with wavelet encoding in 3D GRE sequences. Radiology 201:1254. No. SS.
32. West J, Fitzpatrick JM, Wang MY, Dawant BM, Maurer CR, Kessler RM, Maciunas RJ, Barillot C, Lemoine D, Collignon A, Maes F, Suetens P, Vandermeulen D, van den Elsen PA, Napel S, Hemmier PF, Napel S, Sumanaweera TS, Harkness B, Hemier PF, Hill DLG, Hawkes DJ, Studholme C, Maintz JBA, Viergever MA, Malandain G, Pennec X, Noz ME, Maguire GQ, Pollack M, Pelizzari CA, Robb RA, Hanson D, Woods RP (1997) Comparison and evaluation of retrospective intermodality brain image registration techniques. J Comp Assist Tomogr 21:554–566.
33. Wildermuth S, Debatin JF, Leung DA, Dumoulin CL, Darrow RD, Uhlschmid G, Hofmann E, Thyregod J, von Schulthess GK (1997) MR imaging-guided intravascular procedures: initial demonstration in a pig model. Radiology 202:578–583.